ASYMMETRICAL WATER IMPACT OF TWO-DIMENSIONAL WEDGES WITH ROLL ANGLE WITH MULTI-MATERIAL EULERIAN FORMULATION

(DOI No:10.3940/rina.ijme.2014.a2.280)

S Wang and **C Guedes Soares**. Centre for Marine Technology and Engineering (CENTEC), Instituto Superior Técnico, Universidade de Lisboa, Portugal

SUMMARY

A hydrodynamic study on the asymmetrical water impact of two-dimensional wedges with roll angle is presented. The slam induced loads on the wedges entering calm water with both vertical and horizontal velocities are predicted based on the explicit finite element method. The effects of the horizontal impact velocity and the roll angle are investigated through the predicted results of pressure distribution, pressure variation during the water entry and total impact force, which are also compared with analytical formulations and other numerical calculations. The present method gives reasonable predictions, compared to the numerical and analytical results.

NOMENCLATURE

ρ	Density of water (kg m^{-3})
p	Pressure (N m^{-2})
p_0	Pressure of atmosphere (N m^{-2})
g	Acceleration of gravity (m s^{-2})
η	Water surface (m)
F	Total vertical impact force *(N)*
t	Time instance during impact (s)
C_p	Non-dimensional coefficient of p
C_F	Non-dimensional coefficient of force
σ	Roll angle of the wedge (º)
γ_1	Deadrise angle of the left side of wedge (º)
γ_2	Deadrise angle of the right side of wedge(º)
β	Deadrise angle of the symmetric wedge (º)
B	Breadth of the wedge (m)
L	Length of the wedge(m)
V	Vertical velocity (m/s)
U	Horizontal velocity (m/s)
α	Relative position on the wedge
τ	Time coefficient
ε	Impact velocity ratio

1. INTRODUCTION

Slamming happens when a ship bottom hits the water with a high velocity in rough sea. This slam induced loads can cause local damage to ship hulls and induce global whipping responses. Ship motions and wave induced loads are sometimes calculated by strip theory programs, in which case sectional forces are required and the slamming loads need to be assessed for two dimensional sections corresponding to the ships sections. An example of such an approach is the one adopted by Guedes Soares (1989) who used a method to evaluate the vertical transient load on the ship hull when the forward bottom impacts in water, and later checked it experimentally (Ramos, et al. 2000). They conducted an experimental program assessing the slam induced loads on a segmented ship model, which was analysed with the method used by Ramos and Guedes Soares (1998). These test results have also been used recently to validate CFD calculations by Paik, et al. (2009).

Early studies on the water impact focused on the analysis of two-dimensional and symmetric structures. The important pioneering study on this subject can be attributed to von Kármàn (1929) who proposed the first theoretical method on the analysis of seaplane landing. Then, Wagner (1932) proposed an asymptotic solution for water entry of two-dimensional bodies with small local deadrise angles, accounting for piled-up water on the wedge by simply introducing a constant surface wetting factor C_w, which results in overestimation on the impact load. Armand and Cointe (1987) and Howison et al. (1991) developed this work by accounting for the effect of nonlinear jet flow in the intersection region between the body and free surface using asymptotic matching. For the idealized case of a wedge entering the calm water, Dobrovol's skaya (1969) derived an analytical solution by transferring the potential flow problem for the constant water entry into a self similar flow problem in complex plane, which took advantage of the simplicity of the body geometry and is valid for any deadrise angle.

More recently, Zhao et al. (1993) generalized the work of Wagner (1932) and presented a numerical method for studying the water entry of a two-dimensional body of arbitrary cross-section which is a nonlinear element method with a jet flow approximation. As a further development, a fully nonlinear numerical simulation method which includes flow separation from knuckles of a body and an approximation solution which does not include flow separation were presented by Zhao and Faltinsen (1996) to predict slamming loads on two-dimensional sections. They also conducted the drop tests for a wedge with deadrise angle 30º and a bow-flare section. Korobkin and Iafrati (2005) suggested a practical method to derive the initial hydrodynamic loads, by using the results of direct numerical simulations of the floating body impact. This method is not valid for floating bodies with small deadrise angles. Luo et al. (2011) estimated the slamming loads on a rigid wedge by applying an explicit finite element method, which show great agreement with the measured values. Wang et al. (2012a) extended this work to the wedges with different deadrise angle varying from 10º to 80º, and determined the effects of the deadrise angle on the pressure distribution. Then, the predicted force coefficients on the wedges with different deadrise angle were presented in Wang and Guedes Soares (2012b), showing good consistence with the results from Stavovy and Chuang (1976), who obtained the coefficients of peak pressure for the wedges with different deadrise angles according to experiments results, and Ochi and Motter (1973) who obtained the slamming loads in terms of slamming pressure, the pressure distribution and the time variation of the total slamming load by analysing many test results.

Water impact problem with no constant velocity has also been considered in a number of publications. Through an approximation and matching between the inner solution and outer solution, Faltinsen (2002) extended his equations to variable speed cases, but for his scheme the force at the current step is calculated by using the acceleration at the last time step. Wu et al. (2004) adopted the method of using the auxiliary functions developed by Wu (1998), which allows one to work out the body acceleration before the force is found. Yettou (2007) presented an analytical solution to symmetrical water impact problems of a two-dimensional wedge by taking into account the effect of velocity reduction of the solid body upon impact.

Most investigations of water entry problems, including the researches mentioned above have been focused on the symmetric or vertical impact, and much less work has been conducted on the oblique cases. In the field of oblique water entry, Xu et al. (1998) proposed a theory for asymmetric impact problems of vessels that was a further development of Vorus (1996) work. Korobkin (2005) introduced a model to solve the two-dimensional problem of a wedge with roll angle entering water at a constant vertical velocity. Their models considered only vertical impact, which means that the horizontal component of velocity is zero. By employing the method of two-dimensional vortex distribution and an iterative technique, Judge et al. (2004) examined initial asymmetric water entry flows with horizontal as well as vertical impact velocity. Zhu et al. (2005) studied the water entry of heeled ship sections using CIP method, and then Xu et al. (2008) numerically simulated the wave elevation, pressure distribution and force for a wedge with different roll angle and various horizontal components of impact velocity.

Stenius et al. (2006) examined the ability of an explicit finite element method to study the 2D fluid-structure interaction problem, and investigated the effects of the contact stiffness and mesh size on the numerical results, based on an ALE formulation. By applying the same method, Wang and Guedes Soares (2013) evaluated the slam induced loads on two-dimensional bow-flared sections with different roll angles during water entry. Their numerical results agree well with the measure values from the drop tests of Aarsnes (1996) and the predictions from the BEM of Sun and Faltinsen (2009).

This explicit finite element method is applied in this work to investigate the asymmetrical water impact of a rigid wedge with roll angles, which covers the problems of symmetric wedge entering water with various roll angles and an oblique wedge entering water with both horizontal and vertical impact velocities. In this fluid-structure coupling algorithm, two superimposed meshes are considered, a fixed Eulerian or ALE mesh for the fluid and a deformable Lagrangian mesh for the structure. Unlike existing algorithms that couple two separate codes, a CFD and a structure code, this fluid-structure algorithm described in Aquelet et al. (2005) is fully coupled. The main purpose of this paper is the application of this method to the asymmetrical water entry of 2D wedges. The predicted pressure distribution and time histories of forces are compared with available results from other solutions, and the effects of the roll angle and the horizontal velocity on the hydrodynamic loads on the section are examined according to the predictions.

2. NUMERICAL METHOD

2.1 DESCRIPTION OF THE PROBLEM

An asymmetric water entry of a two-dimensional wedge with a left deadrise angle γ_1 and a right deadrise angle γ_2 is shown in Figure 1. The roll angle σ, which represents the asymmetry, equals to $(\gamma_2 - \gamma_1)/2$, and the deadrise angle of the symmetric wedge is $\beta = (\gamma_1 + \gamma_2)/2$. In the figure *B* is the breadth, *L* is the length of the section, and C.L means the symmetric line of the section. Consider a Cartesian coordinate system *(y, z)*, for which the y-axis is placed in the undisturbed water surface, while the z-axis is located in the symmetric line of the wedge. The wedge enters the calm water at a constant velocity *V* in the *z*-direction, and *U* in *y*-direction, respectively. The boundaries of the water are denoted as SL, SR and SB.

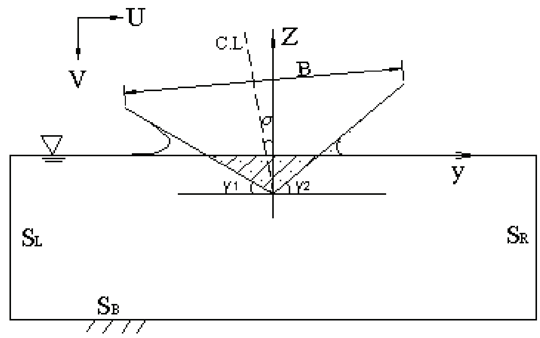

Figure 1. Sketch of the problem

During the water impact, the wedge moves forward in two directions, and the free surface elevations on two sides of the section are different due to the asymmetry. To present the pressure distribution on the relative position of the section surface, consider:

$$\alpha = (y - Ut)/Vt \tag{1}$$

where y is the horizontal coordinate of the section surface and t is the time instant during the impact.

$$\tau = Vt/0.5B \tag{2}$$

where $t=0$ means the time instant when the section touches the water during the impact, and the force coefficients are represented as:

$$C_F = F/0.5\rho BV^2 \tag{3}$$

where F is the total impact force on the section and ρ is density of water.

2.2 GOVERNING EQUATIONS AND BOUNDARY CONDITIONS

In Arbitrary Lagrangian-Eulerian (ALE) formulation, a reference coordinate which is not the Lagrangian coordinate and Eulerian coordinate is induced. The differential quotient for material with respect to the reference coordinate is described as following equation:

$$\frac{\partial f(\vec{X},t)}{\partial t} = \frac{\partial f(\vec{x},t)}{\partial t} + \vec{w}\frac{\partial f(\vec{x},t)}{\partial x} \tag{4}$$

where, $\vec{X}$ is Lagrangian coordinate, $\vec{x}$ is Eulerian coordinate, and $\vec{w}$ is relative velocity between the particle velocity $\vec{v}$ and the velocity of the reference coordinate $\vec{u}$. Therefore, the ALE formulation can be derived from the relation between the time derivative of material and that of the reference geometry configuration.

Let $\Omega^f \in R^3$ represent the fluid domain, and $\partial\Omega^f$ denote its boundary. The equation of mass, momentum and energy conservation for a Newtonian fluid in ALE formulation in the reference domain, are given by:

$$\frac{\partial \rho}{\partial t} = -\rho div(\vec{w}) - \vec{w}\cdot grad(\rho) \tag{5}$$

$$\sigma\frac{\partial \vec{v}}{\partial t} = \overrightarrow{div}(\overline{\overline{\sigma}}) + \vec{f} - \rho\vec{w}\cdot\overline{\overline{grad}}(\vec{v}) \tag{6}$$

$$\rho\frac{\partial E}{\partial t} = \overline{\overline{\sigma}} : \overline{\overline{grad}}(\vec{v}) + \vec{f}\cdot\vec{v} - \rho\vec{w}\cdot\overrightarrow{grad}(E) \tag{7}$$

where ρ is the fluid density, f is the body force and σ is the total Cauchy stress given by:

$$\overline{\overline{\sigma}} = -p\cdot\overline{\overline{Id}} + \mu\left(\overrightarrow{grad}(v) + \left(\overrightarrow{grad}(v)\right)^T\right) \tag{8}$$

where p is the pressure and μ is the dynamic viscosity. The part of the boundary at which the velocity is assumed to be specified is denoted by $\partial\Omega_1^f$, the inflow boundary condition is:

$$\vec{v} = \vec{g}(t) \text{ on } \partial\Omega_1^f \tag{9}$$

The traction boundary condition associated with equation (6) is the condition on stress components. These conditions are assumed to be imposed on the remaining part of the boundary:

$$\overline{\overline{\sigma}}\cdot\vec{n} = \vec{h}(t) \text{ on } \partial\Omega_h \tag{10}$$

The Multi-Material Eulerian formulation is classed as part of the ALE solver, which involves a Lagrangian step, where the mesh is allowed to move and a second step that advects the element state variables back onto a reference mesh. The multi-material Eulerian formulation is a specific ALE case where the reference mesh velocity is zero, which means:

$$\vec{u} = 0 \tag{11}$$

Let $\Omega^s \in R^3$, the domain occupied by the structure, and let $\partial\Omega^s$ denote its boundary. A Lagrangian formulation is considered, so the movement of the structure Ω^s described by $x_i(t)(i=1,2,3)$ can be expressed in terms of the reference coordinates $X_\alpha(\alpha=1,2,3)$ and time t

$$x_i = x_i(X_\varepsilon, t) \tag{12}$$

The momentum equation is given by:

$$\rho\frac{d\vec{v}}{dt} = \overrightarrow{div}(\overline{\overline{\sigma}}) + \vec{f} \tag{13}$$

where ρ is the fluid density, f is the force density and σ is the total Cauchy stress. The solution of equation (13) satisfies the displacement boundary condition equation (14) on the boundary $\partial\Omega_1^s$ and the traction boundary condition equation (15) in the boundary $\partial\Omega_2^s$.

$$\vec{x}\left(\vec{X},t\right)=\vec{D}\left(t\right) \text{ on } \partial\Omega_1^s \tag{14}$$

$$\overline{\overline{\sigma}}\cdot\vec{n}=\vec{\tau}(t) \quad \text{ on } \partial\Omega_2^s \tag{15}$$

where $\vec{n}$ is the unit normal oriented outward at the boundary $\partial\Omega^s$, $\vec{D}(t)$ is the displacement vector and $\vec{\tau}(t)$ is the traction vector.

2.3 NUMERICAL MODELLING

The explicit finite element analysis is based on a multi-material Eulerian formulation and a penalty coupling method. The fluid is solved by using an Eulerian formulation, while the wedge is described by a Lagrangian approach. The fluids (water and air) are defined as the multi-material group, which means that the effects of the water and the air are all considered. The penalty coupling algorithm that behaves like a spring system is applied to activate the interaction between fluids and the structure. The commercial code LS-DYNA is used as a tool to solve the differential equations that govern the phenomenon with following hypotheses: the gravity effects are neglected; the surface tension effects are not modelled; the structure has no deformation or roll motion.

The fluid, water and air, are modelled with Solid164 element which is an 8-nodes brick element, and they are defined as void materials which allows equations of state to be considered without computing the deviatoric stresses. Viscosity of fluid is neglected in this work. The wedge is modelled with Shell163 element which is a 4-nodes element and can only be used in explicit dynamic analysis, and rigid body material.

Since the water entry becomes asymmetric, the full model is established without symmetric boundary as suggested by Wang et al. (2011). The boundaries of the water which are denoted as SL, SR and SB in Figure 1 are defined as non-reflecting. All nodes are fixed in x-direction because of the two-dimensionality. For the wedge, only translational movements along y and z-direction are released.

As known, the ALE calculation is time-consuming, so different mesh types are applied on different regions to reduce memory and CPU requirement. A convergence study of the mesh size, penalty factor and time step were conducted by Luo et al. (2011), who found that the mesh size in the region near the contact area between the structure and the fluids are of great importance to the simulation. As to the region that is far from the impact, the mapped area mesh which contains only quadrilateral elements is employed, and the mesh size in this domain is moderately expanding towards the boundaries.

Figure 2 shows the numerical modelling of the problem. Considering the computational efforts, the fluids domain is limited to *(0.2m+0.7m)*2.5m*, which means the dimension of air domain *(L1*L3)* is *0.2m*2.5m* and that of fluid domain is L2*L3 *(0.7m*2.5m)*. The dimension of impact domain *(L4+L5)*L6* is *(0.1m+0.2m)*0.8m*, and this region is denoted as Domain A. Kaushik and Romesh (2011) studied the effects of the penalty stiffness parameter k_d and mesh size on the pressure coefficients of rigid wedges with different deadrise angles. They found that, the optimum values of the contact stiffness k_d for the wedges with $\beta=10^{\circ}$, $\beta=30^{\circ}$ and $\beta=45^{\circ}$ are 12.5*Gpa/m*, 1.25 *Gpa/m* and 1.25 *Gpa/m*, and very small mesh size is required to capture the peak value of pressure on the wedge with a small deadrise angle. In the present work, the left and right deadrise angle is different due to a roll angle, and the smaller one is also smaller than β. The biggest roll angle in this work is 20º, which means for the wedge with $\beta=60^{\circ}$, the smallest deadrise is 40º, and for the wedge with $\beta=25^{\circ}$, the smallest deadrise is 5º. Therefore, 12.5*Gpa/m* is selected for the wedges with deadrise angle below 45º, and 1.25 *Gpa/m* is selected for the cases with 45º and over.

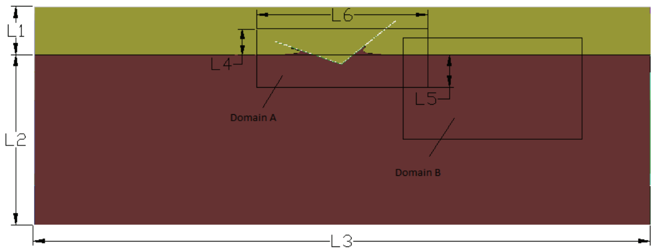

Figure 2. Numerical modelling of the problem.

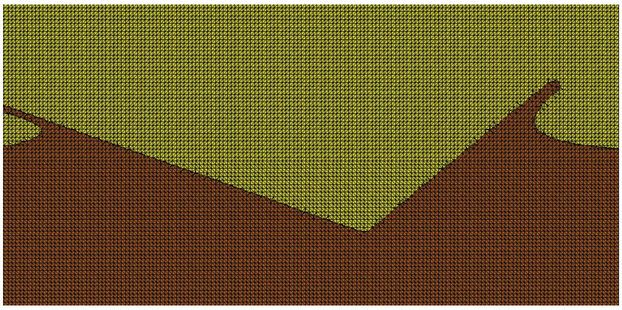
Figure 3. Detail mesh in domain A.

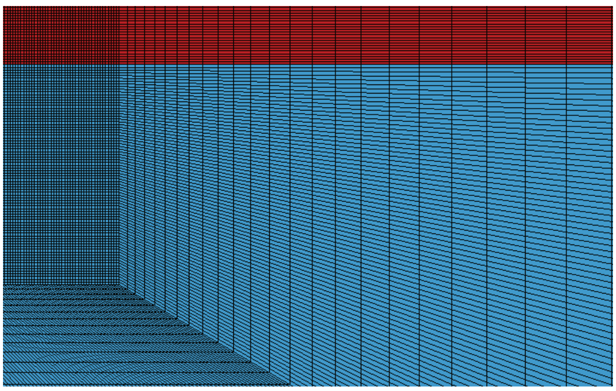
Figure 4. Detail mesh in outer domain of fluids.

The domain A is uniformly meshed with 240*640*1 solid elements as plotted Figure 3, and the structure is meshed with 460 shell elements. The outer domains of fluids (Domain B in Figure2) are meshed moderately expanding towards the boundaries as illustrated in Figure 4.

3. RESULTS AND DISCUSSION

3.1 WEDGES WITH DIFFERENT ROLL ANGLES

To study the effects of the roll angle on the pressure distribution and impact force for wedges with different deadrise angle, the special cases of water entry with only vertical velocity are considered here.

3.1 (a) Pressure distribution

Semenov and Iafrati (2006) proposed an analytical solution for the water entry when U=0, the results from which have been compared with the numerical values from Xu (2008) for the cases when the deadrise angle is 30º and 60º respectively. As plotted in Figure 5 and Figure 6, the predicted pressure distributions from LS-DYNA for these two cases are compared with their results. The two different roll angles, σ=10° and σ=20° are considered. The pressure coefficient is given as $C_p = p / \rho V^2$, where p is the pressure on the wetted surface, and V is the vertical impact velocity. The relative position on the section surface is denoted by α (see eq.(1)), where α =0 means the keel of the wedge.

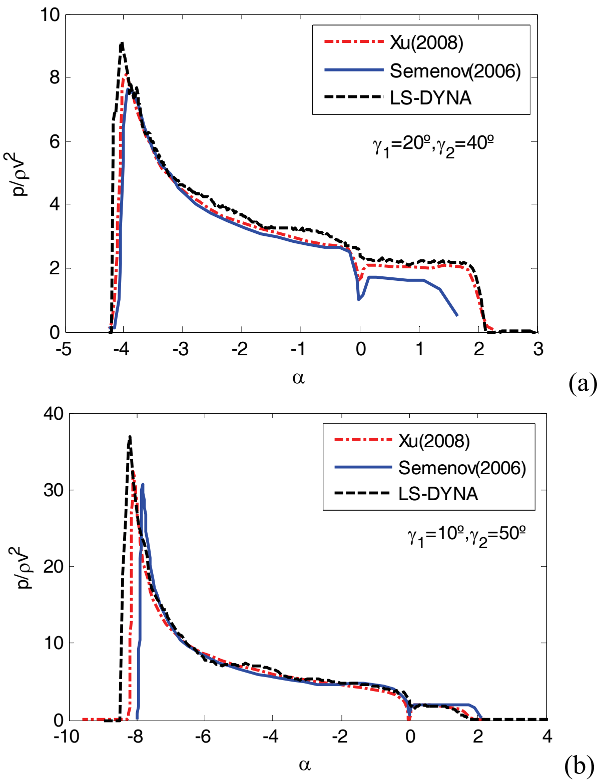

Figure 5. Pressure distributions on the surfaces of wedges with deadrise angle 30º.

As seen in these two figures, the overall agreements between the numerical results are quite good. For the wedge with $\beta = 30^{\circ}$, the maximum coefficients on the left side for both the cases with $\sigma = 10^{\circ}$ and $\sigma = 20^{\circ}$ are slightly higher than the calculations from Semenov (2006) and Xu (2008), and the wetted length of the structural surface in present work is larger. For the pressure coefficients on the right side, the results from present method is in very good agreement with the ones from Xu (2008), while the calculations from Semenov (2006) are much lower for $\sigma = 10^{\circ}$ and higher for $\sigma = 20^{\circ}$. For the wedge with $\beta = 60^{\circ}$, the values from different methods have good consistency on the left side, especially near the water jet flow, though the numerical results in this work have some noises and are slightly higher near the keel. For the pressure coefficients on the right side, the predicted values near the keel are much lower than other results. It means that the air pocket at the keel is probably produced due to the asymmetry in the water entry.

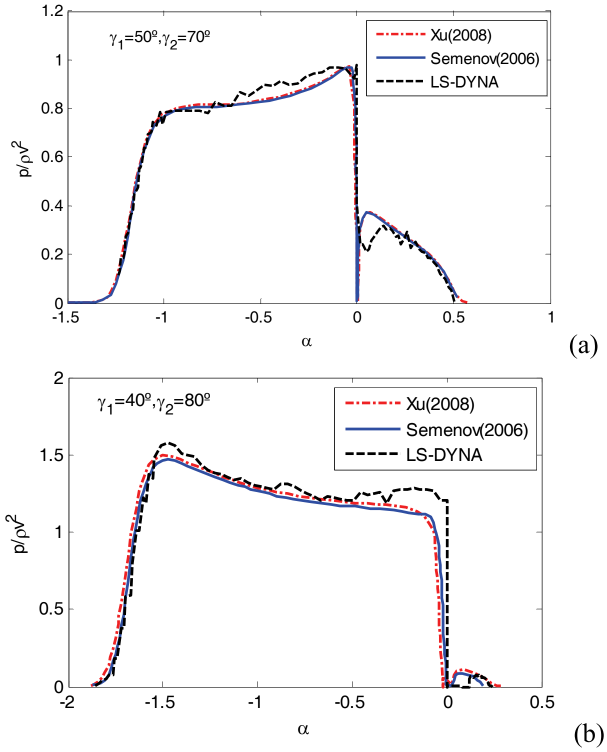

Figure 6. Pressure distributions on the surfaces of wedges with deadrise angle 60º.

In general, the peak value is located at the spray root of the water jet for the wedges with $\gamma 1=20^{o}$, $\gamma 2=40^{o}$ and $\gamma 1=10^{o}$, $\gamma 2=50^{o}$. For the wedge with $\gamma 1=50^{o}$, $\gamma 2=70^{o}$, the peak value is locate at the keel. For the wedge with $\gamma 1=40^{o}$, $\gamma 2=80^{o}$, the peak value is located at the spray root of the water jet. Obviously, the pressure on the left side is larger than that on the right side because the left deadrise angle γ_1 is smaller than the right deadrise angle γ_2. At a given deadrise angle, the pressure on the left side becomes higher as the increasing roll angle, while that on the right side decreases. This is consistent with the fact that the pressure increases as the deadrise angle becomes smaller for the symmetric case.

3.1 (b) Pressure distribution

Algarin and Tascon (2011) compared the calculated pressure distribution and impact force for rigid wedges with $\beta=20^o$, $\sigma=-10^o$ and $\beta=25^o$, $\sigma=-5^o$ to the results from Toyama (1993) and CFD modelling by Star CMM+. For the work of Algarin and Tascon (2011), it is assumed that the asymmetric geometry does not affect the jet velocity and the flow separation from the knuckle in one side does not affect the value of the half beam in another side. Toyama (1993) extended the model of Wagner (1932) for the asymmetric water entry based on expanding flat plate approximation, however, flow separation was not considered. It must be noted that the roll angle here is negative here due to the clockwise rotation of the section. Their results are compared with the predicted values from LS-DYNA in Figure 7. As mentioned before in equation (2), τ represents the time coefficient during the impact. Figure 7 (a), (b), and (c), respectively, plot the pressure distributions when $\tau=0.1$, $\tau=0.2$, and $\tau=0.4$, where $\tau=0.1$ means the time moment before flow separates from the right side, τ=0.2 means the time moment before flow separates from the left side, and τ=0.4 is the time moment after flow separates from both sides.

As plotted in Figure 7(a) and (b), the various methods give consistent predictions on the middle part of the structural surface, while peak values have some differences. At the first time moment, the predicted peak value from CFD is much lower than the other calculations. At the second time moment, the peak pressure in the present work is higher than the ones from CFD and Algarin (2011). From the results of the positions where the zero values occur, the estimated half-wetted lengths of the surface can be known. As seen in Figure 7(a), the zero pressures occur between $x/0.5B=0.8$ and $x/0.5B=0.9$ on the right side of the wedge, and they appear between $x/0.5B=0.3$ and $x/0.5B=0.4$ on the left side. The CFD approach gives the longest half-wetted length on both sides. The half-wetted length on the right side obtained from LS-DYNA is shorter than that from Toyama (1993), and the one on the left side is longer than that from Toyama (1993). At the second time moment (see Figure 7 (b)), the half-wetted length from Algarin (2011) is shorter than other results on the left side, while the right part of the structure is fully-wetted. At the first and second moment, the lower peak pressures from CFD method are probably due to the mesh size and the pressure frequency applied in the simulations. As seen in Figure 7(a), the peak pressure on the right side from Algarin (2011) is higher, and the value from left side is lower. It is caused by the assumption of asymmetric geometry does not affect the jet velocity, which means the peak value on the right side is the same like the one from the symmetric case with a deadrise angle of 10º and the peak value on the left side is similar to the value from the symmetric case with a deadrise angle of 30º. Actually, because $\gamma_1 > \gamma_2$, the pressure on right side is higher before flow separation, thus the fluid will be pushed towards the left side. As a result, the peak pressure on the left side would be higher than the symmetric one, while the value on the right side would be lower. This is also the reason for the discrepancies of pressure at the second moment.

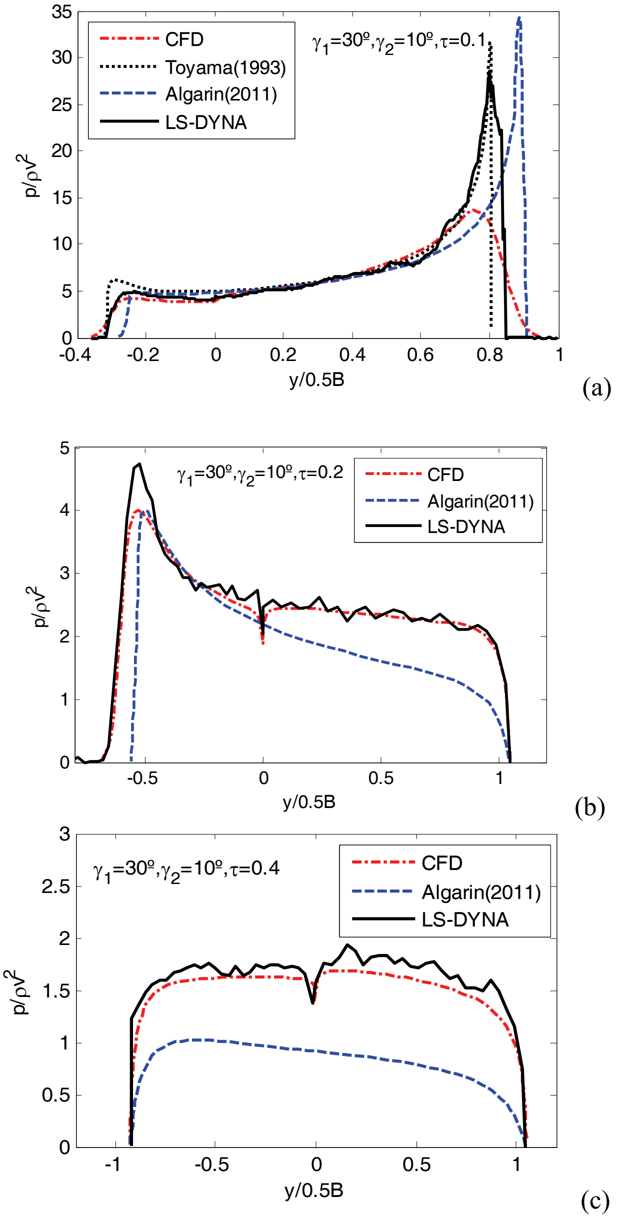

Figure 7. Pressure distributions during water impact for β=20º, σ=-10º

Another important parameter of the water impact problem is the wetted factor, which is defined as $C_w = (1+z_{max}/Vt)$, where z_{max} means the vertical coordinate of the position of peak pressure on the wetted surface and it can be given as $z_{max}=y_{max}\tan\gamma i(i=1,2)$. Therefore, the quantitative description of C_w can be found based on $y_{max}/0.5B$ in Figure 7. Here, the left wetted factor is defined as C_{w1} and the right wetted factor as C_{w2}. As seen in Figure 7(a), the value of C_{w1} from Algarin (2011) is the smallest due to the assumption that the flow separation from the knuckle in one side does not affect the value of the half beam in another side, while the values from LS-DYNA and CFD agree well. The values of C_{w2}

from CFD, LS-DYNA and Toyama (1993) have good consistency. In Figure 7(b), it can be found that the values of C_{w1} are in good agreement for these methods. As plotted in Figure 7(c), the present method gives about 50% larger pressures than Algarin (2011). The results from present work are believed more reasonable, because the comparisons of the pressure distribution at late stage for a symmetric case with $\beta = 30°$ (see figure 5 of Algarin (2011)) shows the limilation of the model on predicting the pressures after flow separation.

In general, at the first time moment $\tau=0.1$, the peak value is located near the spray root of the water jet on the right side of the wedge with deadrise angle 10º. At the second time moment $\tau=0.2$, the pressure on the right side decreases greatly due to the flow separation, and the peak value moves to the spray root of the water jet on the left side. At the third time moment $\tau=0.4$, the pressure drops overall, because the flow separates from both sides of the wedge and the structure immerses under the water completely.

For the wedge with $\beta=60°$, $\sigma=20°$, the pressure variation on the wetted surface during the impact is illustrated in Figure 8, which includes the curves at three time moments of the impact. On the oblique side (here means the left side), the peak value of pressure is located near the spray root of the water jet at the first time moment, and then it decreases and moves to the keel of the wedge after flow separation on this side. On the right side, the pressures are much lower than those on the left side during the entire impact process, and some zero-pressure regions are observed at the keel. The size of the zero-pressure region on the section surface increases as the wedges enters. It is probably due to the evolution of air pocket.

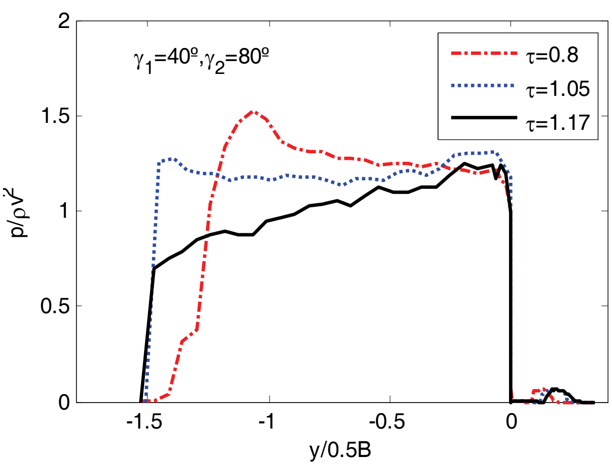

Figure 8. Pressure distributions during water impact for the wedge section with β=60º, σ=2.

3.1 (c) Water surface elevation and pressure contour

Corresponding to the calculated pressure distributions at the different time moments mentioned above, the pressure contours at those time moments are plotted in Figure 9 and Figure 10, together with the free surface elevations.

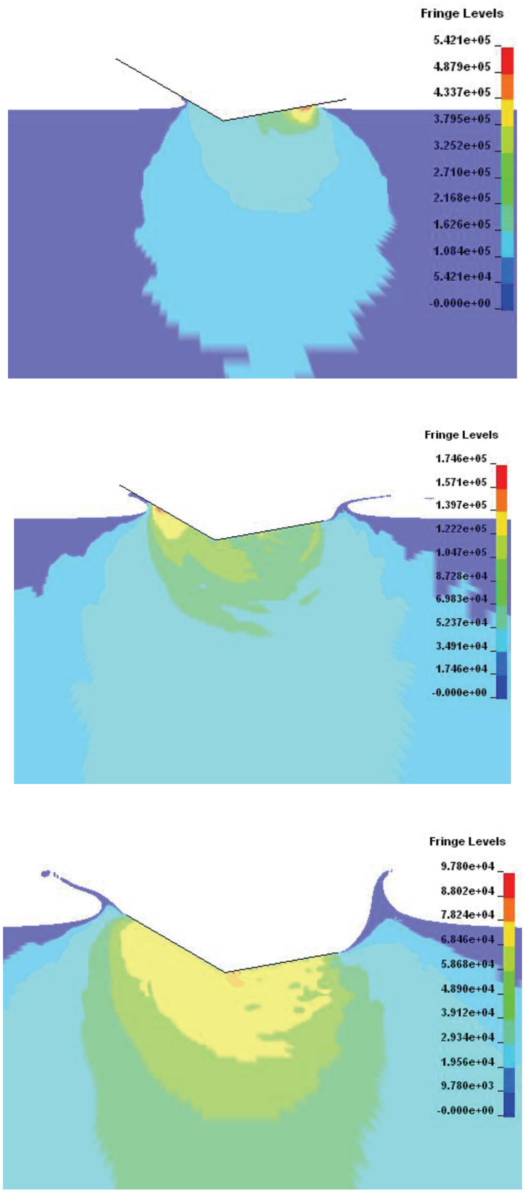

Figure 9. Water surface elevation and pressure contour during water impact for β=20º, σ=-10º

Since the simulated free surface elevation depends, to some extent, on the mesh size, the fluids domain and maybe some uncertain factors of the model, it cannot be predicted as precisely as in the real situation, but it can be qualitatively estimated for its evolution during the water entry. As plotted, the pressure contours at different time instants are in good agreement with the predicted pressure variations mentioned above as shown in Figure 7 and Figure 8. As seen in Figure 10, a very small air pocket is observed on the right side of the wedge section with $\beta=60°$ and $\sigma=20°$. As the wedge drops downwards, the air pocket becomes larger. This phenomenon is consistent with the evolution of zero-pressure region plotted in Figure 8.

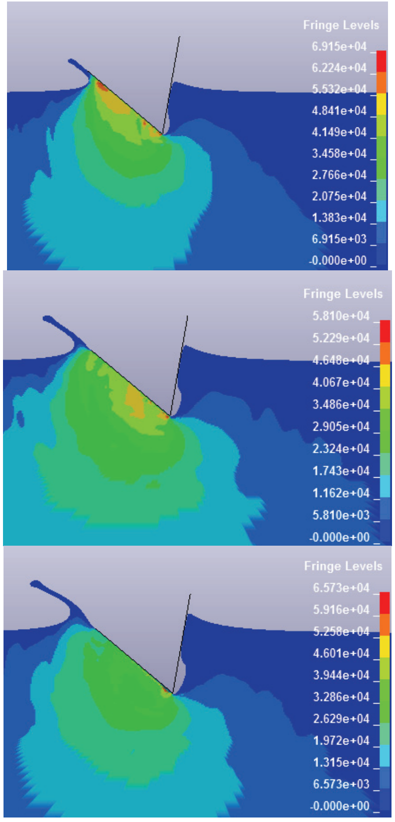

Figure 10. Water surface elevation and pressure contour during water impact for the wedge section with β=60º, σ=20.

3.1 (d) Impact force

Figure 11 compares the predicted vertical and horizontal forces with the results obtained from Algarin and Tascon (2011) and CFD modelling, for a falling wedge with *β=20º*, *σ=-10º*. Good agreement is achieved between these results. At the initial stage, the vertical force from Algarin and Tascon (2011) is slight higher than the values from LS-DYNA and CFD approaches. This is consistent with the results of pressure distributions on the wetted surface at *τ=0.1*, which are shown in Figure 7(a). Since that the impact force is obtained by integrating the pressures along the wetted surface. When *τ=0.2* and *τ=0.4*, the vertical forces from LS-DYNA are higher than other calculations. In present work, the maximum vertical force occurs at *τ=0.123*, which is a little later than other results, and the value of it is larger than the one from CFD. Similarly, for the horizontal force, the present peak value is lower than the one from Algarin and Tascon (2011), and higher than the one from CFD. However, the predicted peak value occurs earlier than the one from Algarin and Tascon (2011).

In general, at the initial stage, the vertical impact forces are almost linearly increasing, until it comes up to the peak value, and they decrease fast after the flow separates from the right side, then reaches a small peak value again and tends to a small value after the flow separates from the left side at the late stage. Due to the asymmetries of the pressure distribution on the wedge section, the horizontal force is produced. As shown in Figure 7(a), the pressure on the right side section is higher than the value on the left side section, so the horizontal force on the wedge is negative at the beginning as plotted in Figure 11 (b). As the flow separates from the right side, the horizontal force decreases and then increases along the positive direction due to the higher pressure on the left side as plotted in Figure 7(b). At the late stage, it decays to a small value as the vertical force does. For this case, it is found that the maximum value of the vertical force is much larger than that of horizontal one.

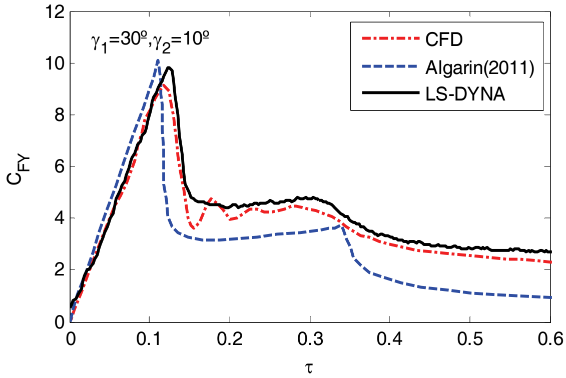

(a)

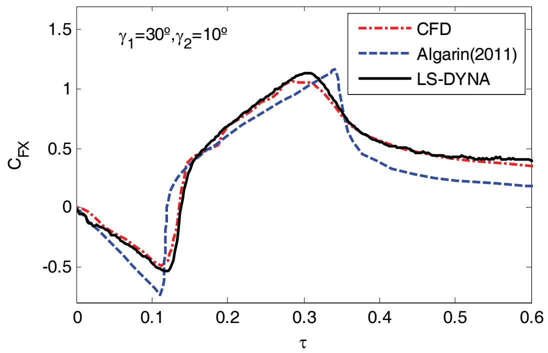

(b)

Figure 11. Time histories of vertical and horizontal forces during water impact for β=20º, σ=-10º. (a) Vertical force coefficient; (b) Horizontal force coefficient.

The comparison of the vertical force for the wedge with *β=25º*, *σ=-5º* is plotted in Figure 12. At the initial stage, the predictions from these methods are in good agreement, except the peak value from CFD is lower and the peak value from Xu (1998) appears later. At the late stage, the vertical forces from LS-DYNA are higher than other results.

To study the relationship between the variations of vertical and horizontal force during the impact for different wedge sections, Figure 13 presents the results for the wedge sections with *β=30º*, *σ=10º* , *β=45º*, *σ=10º* and *β=60º*, *σ=10º*. With the same roll angle 10º, the peak value of vertical force is much larger than that of the horizontal force when the deadrise angle is 30º, while the differences between the peak values in two directions are limited for the wedge with $\beta=60^o$. However, the vertical peak force and horizontal peak force occur at almost the same moment for all the cases discussed here.

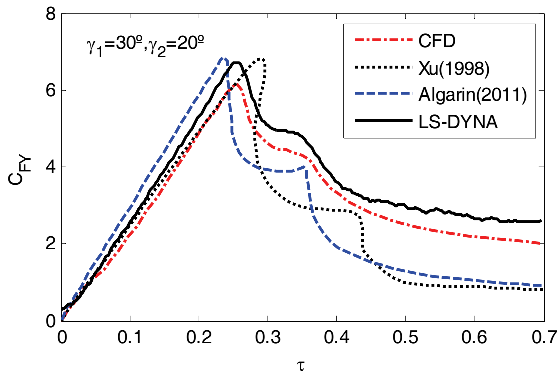

Figure 12. Time history of vertical force during water impact for β=25º, σ=-5º.

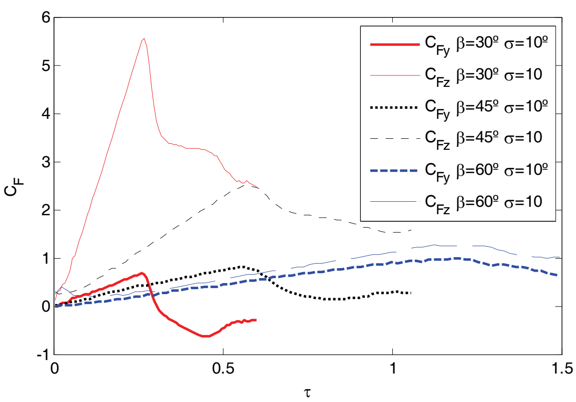

Figure 13. The relationship between the time histories of vertical force and horizontal force for different cases.

In Figure 13, it is also observed for the case of $\beta=30^o$, $\sigma=10^o$ that the horizontal force has a negative peak value at the late stage which is even larger than the peak appeared at the initial stage. Furthermore, the negative peak value decreases as the deadrise angle β increases, even disappears for a larger deadrise angle. The result shows that, for the wedge with a small deadrise angle, the horizontal force at the late stage of the water impact cannot be neglected.

The relationship between the non-dimensional force and the roll angle for the wedge sections with different deadrise angles is plotted in Figure 14. Figure 14(a) includes the numerical results calculated by Korobkin and Malenica (1992) for the case of $\beta=20^o$. The agreement between the predictions of LS-DYNA and those of Korobkin and Malenica (1992) is quite good.

These figures show that the vertical force on the section is larger than the horizontal one, and the differences between them decrease when the deadrise angle β is larger for a constant roll angle, while for a given wedge section, the impact forces become larger as the roll angle increases.

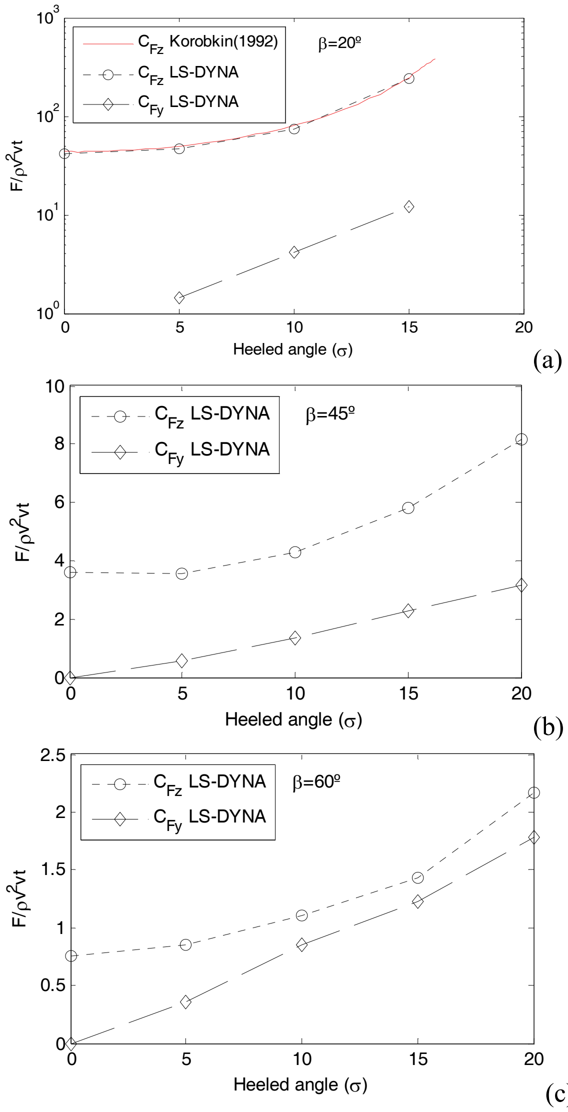

Figure 14. The non-dimensional force coefficients as function of the roll angle for the wedges with different deadrise angle.

3.2 WEDGES WITH HORIZONTAL VELOCITY

The wedge sections entering water with both vertical and horizontal velocity are investigated. The impact velocity ratio is defined as $\varepsilon=U/V$, where U and V are constant values, and $V=6.15$ *m/s* for all the cases studied.

3.2 (a) Pressure distribution

Figure 15 shows the pressure distributions on a symmetric wedge with $\beta=45^o$ entering water with both vertical and horizontal velocities. The ratio of the impact velocity ranges from 0 to 0.5, the results for which are plotted respectively in Figure 15(a), (b), (c) and (d).

The present predictions agree well with the results from Xu et al. (2008). The pressures from LS-DYNA are slightly higher than Xu et al. (2008)'s results. The differences are more apparent near the keel on the right side. As seen from these figures, the pressures on the right side are higher than those on the left side due to the horizontal velocity, and the differences between them become larger for a larger ε.

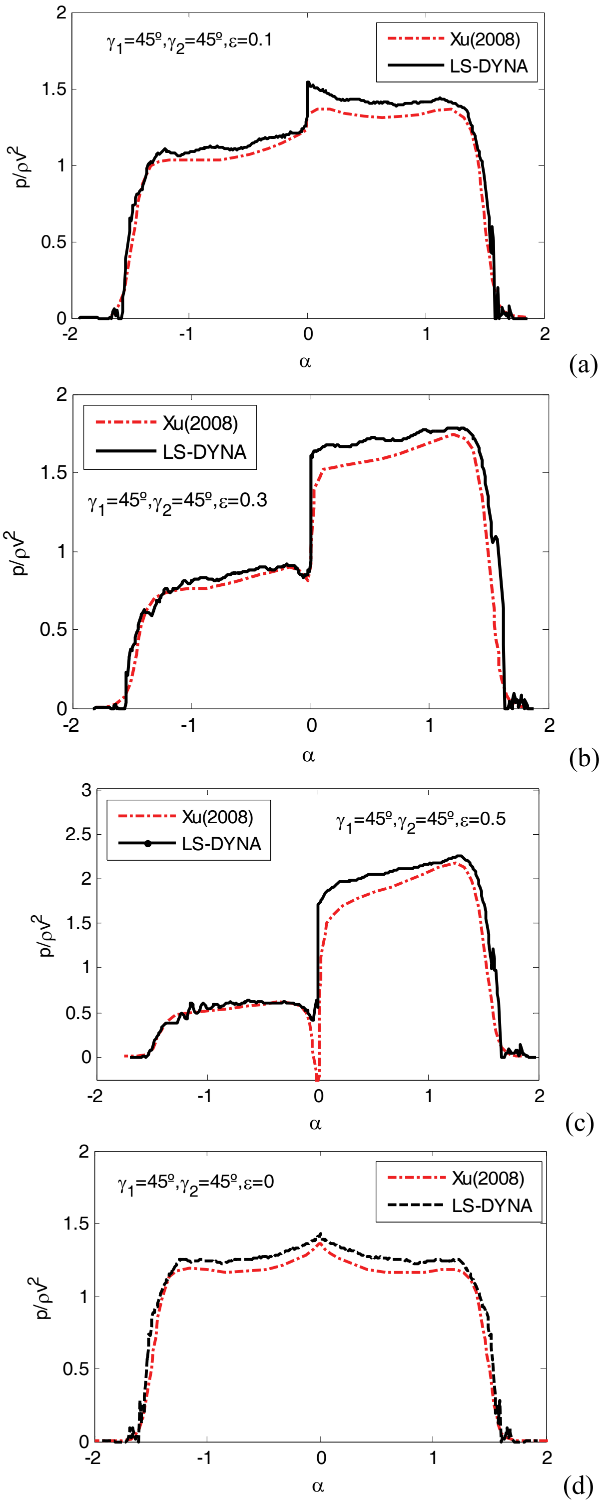

Figure 15. Oblique water entry of a symmetric wedge with β=45º. (a) ε=0.1; (b) ε=0.3; (c) ε=0.5.

With the horizontal velocity, the section has a translational movement towards y-direction, which requires a driving force to push the water out of the way of the section, thus the pressure on the right side increases, while that on the left side decreases.

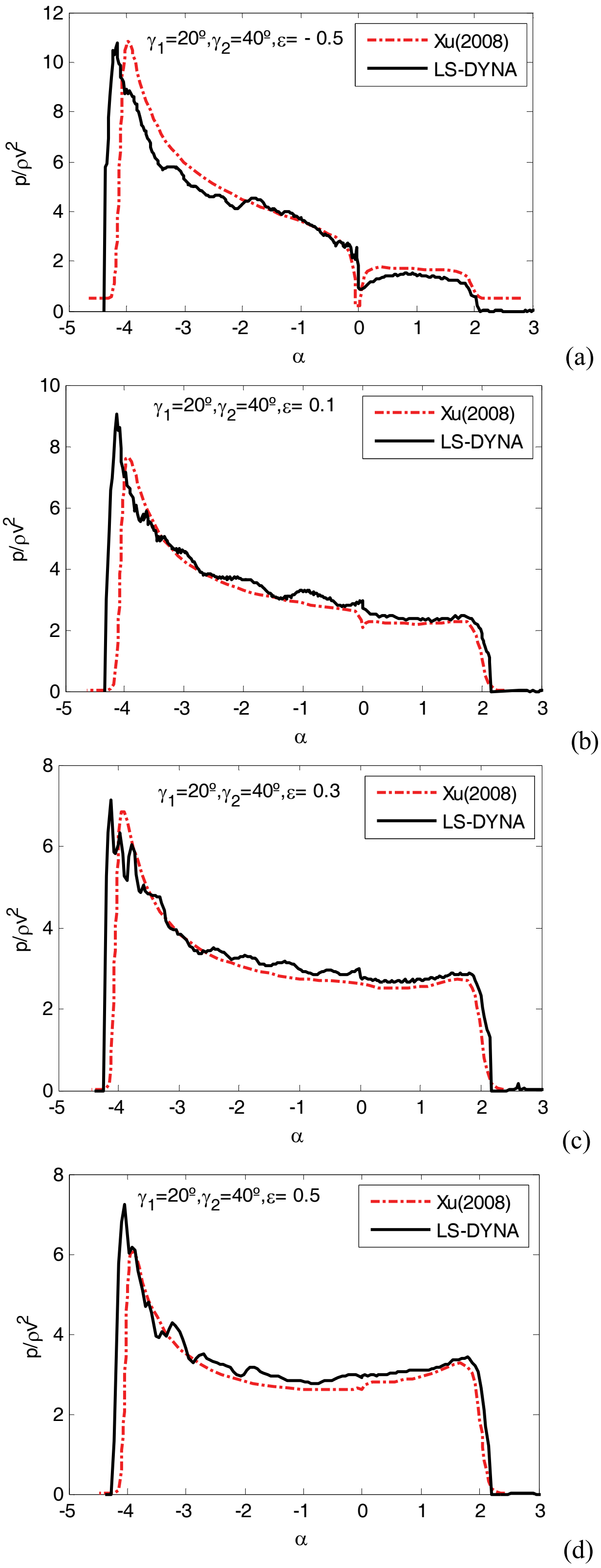

Figure 16. Oblique water entry of a symmetric wedge with β=30º, σ=10º. (a) ε=-0.5; (b) ε=0.1; (c) ε=0.3; (d) ε=0.5.

When the velocity ratio $\varepsilon=0$, and $\varepsilon=0.1$, the peak pressures are located at the keel. When the velocity ratio $\varepsilon=0.3$, and $\varepsilon=0.5$, the peak pressures are located near the spray root of the water jet on right side. The effect of the horizontal velocity seems like the effect of the decrease of the deadrise angle.

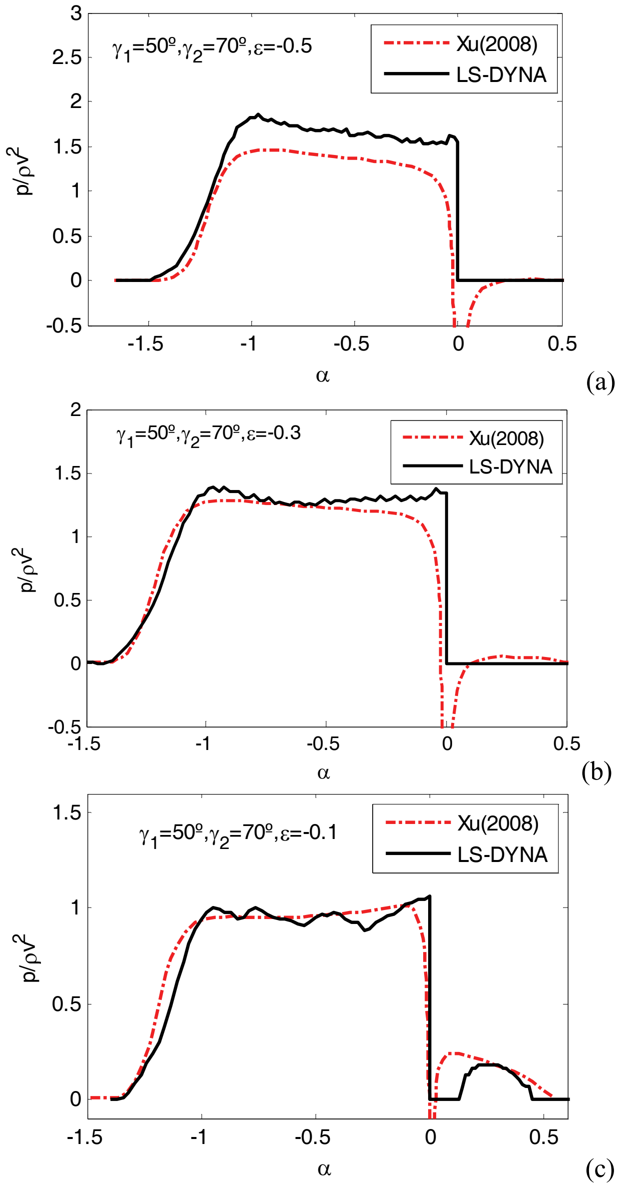

Figure 17. Oblique water entry of a symmetric wedge with β=60º, σ=10º. (a) ε=-0.5; (b) ε=-0.3; (c) ε=-0.1.

Figure 16 and Figure 17 present the pressure distributions on the wedge sections with $\beta=30^o$, $\sigma=10^o$ and $\beta=60^o$, $\sigma=10^o$. Different ratios of velocity $\varepsilon=-0.5$, $\varepsilon=-0.3$, $\varepsilon=-0.1$, $\varepsilon=0.1$, $\varepsilon=0.3$ and $\varepsilon=0.5$ are considered. When the deadrise angle is 30º, the predictions from LS-DYNA agree quite well with the calculations from Xu (2008), while the predicted peak values are slightly higher and the half-wetted lengths are larger than Xu (2008)'s results. As seen in Figure 16(a), the pressures from Xu (2008) are not zero at the ends of the section surface where is not the wetted part. This is probably due to the errors in the data.

For the case of $\beta=60^o$, $\sigma=10^o$, the agreement is less satisfactory. The predicted pressures at the keel are much higher than Xu (2008)'s calculations. When the velocity ratio ε is -0.5, the present approach gives much higher predictions of the pressure on the left side of the wetted surface. For the pressure on the right side, the predicted values in present work are zero for both the cases with $\varepsilon=-0.3$ and $\varepsilon=-0.5$. This means flow ventilation occurs for these cases. When the velocity ratio ε is 0.1, zero-pressure region is observed near the keel on the right side. This is due to the air pocket. For the three cases from Xu (2008) shown in Figure 7, negative pressures are found near the keel. If large negative pressure appears at the keel, ventilation can easily occur, as a result, the pressure on the right side would be zero, however, pressure values are still observed in Figure 17 (b),(c). In their work, the effects of the air pocket that may occur at the keel were not considered.

As the impact velocity ratio increases, the pressure on the left side becomes lower, while that on the right side becomes higher. This can be explained simply like the case with $\beta=45^o$, $\sigma=0^o$ plotted in Figure 15. With a roll angle, the effects of the velocity ration on the differences become more obvious.

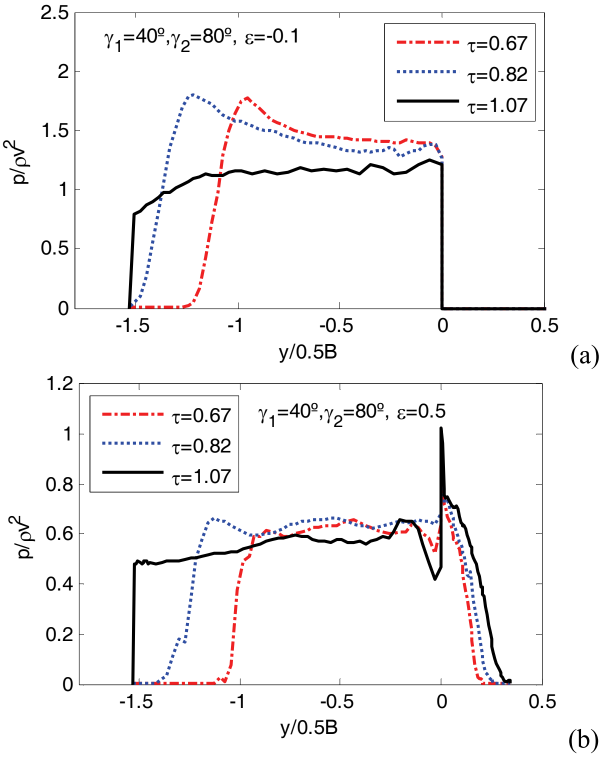

Figure 18. Pressure distribution during the impact for the wedge section with β=60º, σ=20º. (a) ε=-0.1; (b) ε=0.5.

Figure 18 shows the evolution of pressure distribution on the wedge section which has both vertical and horizontal impact velocity during water entry. The impact velocity ratio -0.1 and 0.5 are analysed here.

As seen for the left side of the section, the maximum value of pressure is located near the spray root of the water jet at the beginning of the water impact, and then it decreases after the flow separates from the knuckle of left side and moves towards the keel of the section in the late stage. In short, the variation law of the pressure distribution is similar to that on the wedge section without horizontal velocity. However, the horizontal velocity does have influence on the pressure.

As plotted in Figure 18, the increase of horizontal velocity leads to decrease of the pressure on the left side and increase of that on the right side. Furthermore, it shows that the flow separates from the keel on the right side of the section with $\beta=60^o$, $\sigma=20^o$ when the velocity ratio ε is -0.1. When the velocity ratio ε is 0.5, the pressure at the keel on the right side is very high due to a large horizontal velocity. It is observed that the pressures around the keel on the left side are relatively low. This is due to the relatively low velocity between the fluid and the left side of the section caused by the high horizontal speed towards right direction.

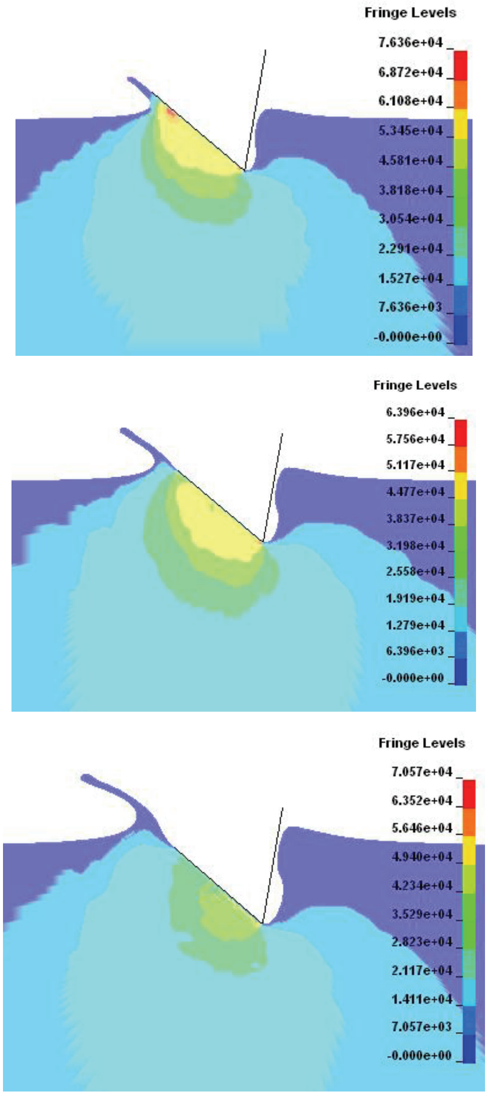

Figure 19. Water surface elevation and pressure contour during the impact for the wedge section with β=60º, σ=20º and ε=-0.1.

3.2 (b) Water surface elevations and pressure contour

As plotted in Figure 19 and Figure 20, the pressure contours at different time instants are in good agreement with the predicted pressure variations mentioned above as shown in Figure 18. For the same wedge section with $\beta=60^o$ and $\sigma=-10^o$, flow ventilation happens when the velocity ratio is -0.1, while it is not observed for $\varepsilon=0.5$.

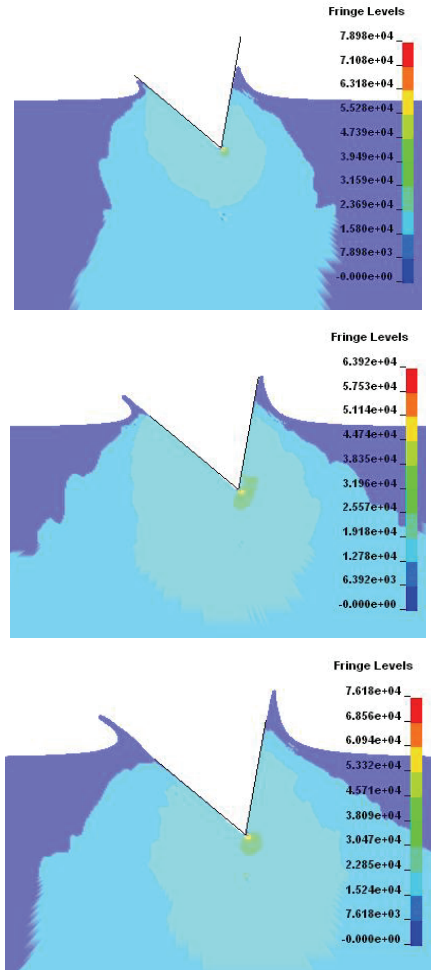

Figure 20. Water surface elevation and pressure contour during the impact for the wedge section with β=60º, σ=20º and ε=0.5.

3.2 (c) Impact force

The time histories of vertical impact force on the wedge section with $\gamma_1=30^o$ and $\gamma_2=20^o$ for different velocity ratio are illustrated in Figure 21, which includes the results from LS-DYNA and the CFD. Similar to the comparisons of the vertical forces on the wedge with the same roll angle but without horizontal velocity as seen in Figure 12, the maximum value of the vertical force obtained from LS-DYNA is a little bit higher than the value calculated by using CFD code. As mentioned before, the peak forces occur when then flow separates from the sides of the section. It is found that the second peak value decreases as the velocity ratio increases for this case.

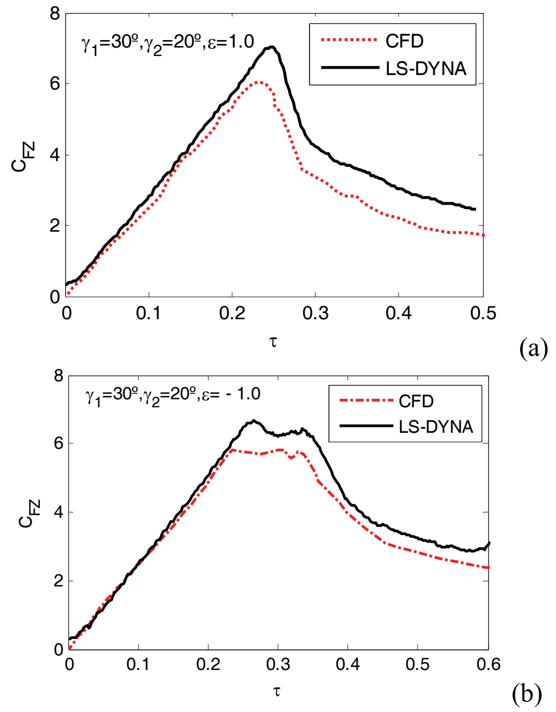

Figure 21. Time history of vertical force during water impact for the wedge section with different impact velocity ratio. (a) γ1=30º, γ2=20º, ε=1.0; (b) γ1=30º, γ2=20º, ε=-1.0.

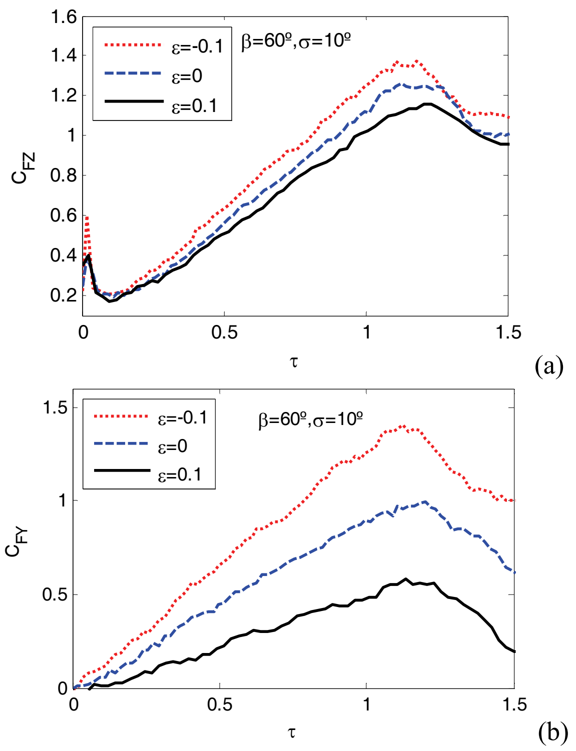

Figure 22. Time history of vertical force during water impact for the wedge section with β=60º, σ=10º and different impact velocity ratios. (a) Vertical force; (b) Horizontal force.

Figure 22 shows the predicted vertical force and horizontal force against the time coefficient for the wedge with β=60º and σ=10º. The cases with the impact velocity ratios -0.1, 0 and 0.1 are considered. The results show that the forces become smaller as the ratio decreases, and the time moment when the flow separates from the section is a little later for a larger velocity ratio. Compared to the vertical force, the influence of the velocity ratio on the horizontal force is more apparent.

To analyse the relative effect of ε on the impact forces for wedge sections with various roll angles, Figure 23 shows both the non-dimensional vertical and horizontal force as functions of velocity ratio ε. The predicted horizontal forces are in quite good agreement with the predictions from Xu (2008), while the predicted vertical forces are higher than Xu (2008)'s values.

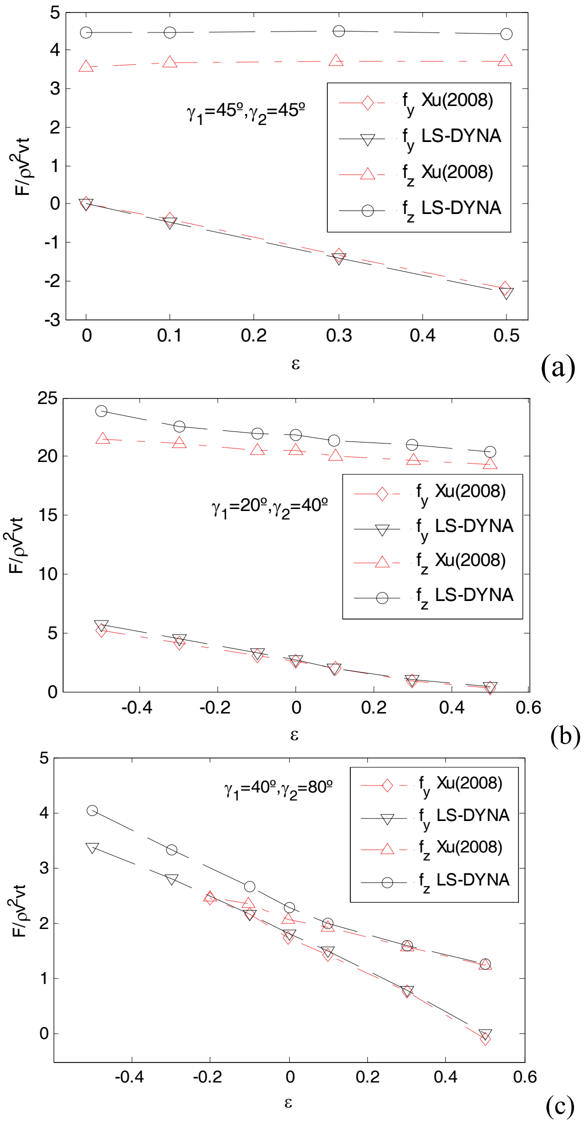

Figure 23. Forces as the function of the velocity ratio ε for different wedge sections.

As seen in Figure 23(a), for the symmetric wedge with β=45º, the effects of ε on the vertical force are very limited, while the absolute value of horizontal force coefficient decreases almost linearly as the velocity ratio ε increase. As to the case of β=30º, σ=10º, which is plotted in Figure 23(b), the force coefficients in the two directions decrease as the velocity ratio ε increases, and the predictions of vertical force from LS-DYNA are higher than those from Xu (2008)'s solution. When it comes to the case with $\beta=60^o$ and $\sigma=20^o$, the effects of ε on the forces are similar to those of the case with β=30º and σ=10º. The vertical forces predicted by LS-DYNA are higher than the values obtained from Xu (2008) when ε is zero and below, and the difference between them becomes more apparent for a smaller ε. In present work, the vertical force coefficients are always higher than the horizontal ones for these three cases. However, for the case with $\beta=60^o$ and $\sigma=20^o$, the vertical force coefficient obtained from Xu (2008) is very close to the horizontal one, when the velocity ratio ε is -0.2. We can imagine that a smaller velocity ratio probably lead to a high horizontal force which is larger than the vertical one.

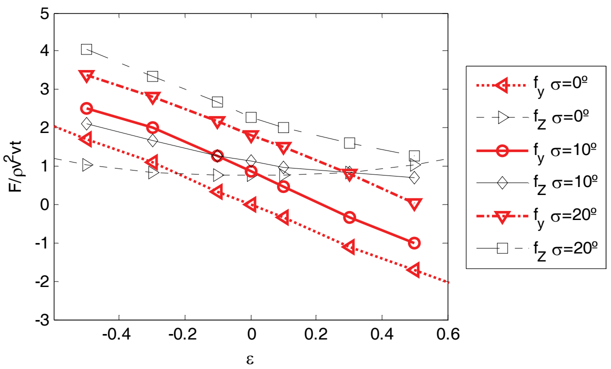

Figure 24. Forces as the function of the velocity ratio ε for the wedge section with β=60º and different roll angles.

Figure 24 shows the non-dimensional forces as the function of the velocity ratio for the wedge section with $\beta=60^{\,o}$. Different roll angles, including 0 º, 10 º and 20 º are considered. It is observed that, for a given deadrise angle β, the horizontal force coefficient is almost linearly decreasing as the velocity ratio increases and the variation ratio of which is nearly stable for different roll angles. The effects of the velocity ratio on the vertical forces are bigger for a larger roll angle.

For the vertical force coefficients, the effects of velocity ratio are small for the case with 0º roll angle. Compared to the wedge section with $\beta=45^o$, on which the vertical force does not change too much for different velocity ratio as plotted in Figure 23(a), the vertical non-dimensional forces are slight higher when a horizontal velocity is applied, for the case with $\beta=60^o$ and $\sigma=0^o$.

When the roll angle is 10º, it is noticed that, for a ε smaller than -0.1, the vertical force becomes smaller than the horizontal one, and the absolute value of which is larger than that of the vertical force for the case with ε 0.5, A similar phenomenon can be found for this wedge section without roll angle, for which the absolute value of the vertical force is smaller than that of the horizontal one when the velocity ratio is larger than 0.3 and smaller than -0.3, however, as illustrated in Figure 23 which corresponds to the symmetric section with $\beta=45^o$, a larger ε is required for this phenomenon.

4. CONCLUSIONS

The slam induced loads on a wedge section impacting water with a roll angle and horizontal velocity are investigated by an explicit finite element method in the present work. The predictions of pressure distributions, time history of impact force and force coefficients are compared with published numerical and analytical calculations. The comparisons show that this method gives relative higher impact loads on the wedges considered, and the CDF approach underestimates the results. For the peak pressure on the wetted surface, high values are captured by the virtual sensors with very low frequency, when the proper mesh size and contact stiffness are used. For some cases, asymmetric water entry leads to the air pocket near the keel on the leeward side, where the pressure is very small, while the pressure on the downward side is very large. This phenomenon may lead to damage on the structure because of the large relative pressure. Compared to Xu (2008)'s method, the phenomenon is more apparent in this work, as seen in Figure 6, 8, 10, 17. All in all, the method used in this paper is conservative.

It is found that the roll angle and horizontal velocity have significant effects on the hydrodynamic loads. Based on the definition of the coordinate system in present work, the vertical and horizontal forces become larger as the roll angle increases, for a wedge without horizontal velocity. For a symmetric wedge, the effects of the horizontal velocity on the vertical force are very small, while the absolute value of the horizontal force is higher for a larger velocity ratio. Besides, the horizontal impact force might be larger than the vertical one for a higher horizontal impact velocity, especially when the deadrise angle β is large.

For the cases considered in this work, the present method gives reasonable predictions and it can be extended to more general cases.

5. ACKNOWLEDGEMENTS

The work has been performed in the scope of the project EXTREME SEAS – Design for Ship Safety in Extreme Seas, (www.mar.ist.utl.pt/extremeseas), which has been partially financed by the EU under contract SCP8-GA-2009-234175.

6. REFERENCES

1. AARSNES J.V. Drop test with ship sections-effect of roll angle. *Report 603834.00.01. Norwegian Marine Technology Research Institute, Trondheim*. 1996
2. ALGARIN, R., TASCON, O. Hydrodynamic modeling of planing boats with asymmetry and steady condition. *Proceedings of the RINA 9th Symposium on High Speed Marine Vehicles*, pp. 1-9, 2011.
3. AQUELET N., SOULI, M. and OLOVSSON, L, Euler–Lagrange coupling with damping effects: Application to slamming problems, *Computer Methods in Applied Mechanics and Engineering*, Volume 195, pp 110-132, 2005.
4. ARMAND JL., COINTE, R. Hydrodynamic impact analysis of a cylinder. Proc. Fifth Inter. *Offshore Mech. and Arctic Engng*. Symp, Tokyo, Japan, Volume 1, pp. 609-634, 1987.
5. DOBROVOL'SKAYA Z.N. On some problems of similarity flow of fluids with a free surface. *Journal of Fluid Mechanics,* Volume 36, pp 805-829, 1969.
6. JUDGE, C., TROESCH, A., PERLIN, M. Initial water impact of a wedge at vertical and oblique angles. *Journal of Engineering Mathematics*, Volume 48, pp 279-303, 2004.
7. FALTINSEN, O.M. Water entry of a wedge with finite deadrise angle. *Journal of Ship Research*, Volume 46, pp 39-51, 2002.
8. GUEDES SOARES, C. Transient Response of Ship Hulls to Wave Impact. *International Shipbuilding Progress*, Volume 36(406), pp 137-156, 1989.
9. HOWISON SD, OCHENDON JR, WILSON SK.. Incompressible water-entry problems at small deadrise angles, *Journal of Fluid Mechanics* Volume 222, pp. 215-230, 1991.
10. KAUSHIK DAS and ROMESH C. BATRA. Local water slamming impact on sandwich composite hulls. *Journal of Fluids and Structures*, Vol. 27, pp 523-551, 2011.
11. KOROBKIN, A.A., IAFRATI, A. Hydrodynamic loads during initial stage of floating body impact. *Journal of Fluids and Structures*, Volume 21, pp 413-427, 2005.
12. KOROBKIN, A.A., MALENICA S. Modified logvinovich model for hydrodynamic loads on asymmetric contours entering water. *20th International Workshop on Water Waves and Floating Bodies*, Oslo, 2005.
13. LS-DYNA, Keyword User's Manual, Livermore Software Technology Corporation, Version 971, May 2007.
14. LUO, H.B., WANG S., GUEDES SOARES C., 2011. Numerical prediction of slamming loads on rigid wedge for water entry problem by an explicit finite element method. *Advances in Marine Structures*, Guedes Soares, C, and Fricke, W., (Eds), Taylor & Francis, UK, pp 41-47.
15. OCHI M.K. and MOTTER L.E. Prediction of slamming characteristics and hull response for ship design. *Transactions SNAME*, Volume 81, pp. 144-190, 1973.
16. PAIK, K.-J., CARRICA, P.M., LEE, D., MAKI, K.. Strongly coupled fluid-structure interaction method for structural loads on surface ships. *Ocean Engineering*, Volume 36, pp. 1346-1357, 2009.
17. RAMOS, J. and GUEDES SOARES, C. Vibratory response of ship hulls to wave impact loads. *International Shipbuilding Progress*, Volume 45(441), pp. 71-87, 1998.
18. RAMOS, J.; INCECIK, A., AND GUEDES SOARES, C. Experimental Study of Slam Induced Stresses in a Containership. *Marine Structures,* Volume 13(1), pp 25-51, 2000.
19. SEMENOV, YU.A., IAFRATI, A. On the nonlinear water entry problem of asymmetric wedges. *Journal of Fluid Mechanics*, Volume 547, pp 231-256, 2006.
20. STAVOVY, A.B., CHUANG, S.L. Analytical determination of slamming pressures for high speed vessels in waves. *Journal of Ship Research*, Volume 20, pp. 190-198, 1976.
21. STENIUS I., ROSN A. and KUTTENKEULER, J. Explicit FE-modeling of fluid-structure interaction in hull-water impacts, *International Shipbuilding Progress*, Volume 53, pp 1031-121, 2006.
22. SUN, H. and FALTINSEN, O.M. Water entry of a bow flare section with a roll angle. Journal of Marine Science and Technology. Vol. 14, pp. 69-79, 2009.
23. TOYAMA, Y. Two-dimensional water impact of unsymmetrical bodies. *Journal of Soc. Naval Arch. Japan*, Volume 173, pp 285-291, 1993.
24. VON KÁRMÀN, T. The impact on seaplane floats during landing. *National Advisory Committee for Aeronatics*, Techinical note No. 321, pp. 309-313, 1929.
25. VORUS, W. S. A flat cylinder theory for vessel impact and steady planing resistence. *Journal of Ship Research*, Volume 40, pp 89-106, 1996.
26. WAGNER, H. Uber Stossund Gleitvergange an der Oberflache von Flussigkeiten. *Zeitschrift fuer Angewandte Mathematik und Mechanik*, Volume 12, pp 193–215, 1932.
27. WANG, S., LUO, H.B., GUEDES SOARES, C. Explicit FE simulation of slamming load on rigid wedge with various deadrise angles during water entry. *Maritime Technology and Engineering*, Guedes Soares, C, et al. (Eds), Taylor & Francis, UK, pp 399-406, 2012a.
28. WANG, S., GUEDES SOARES, C. Analysis of the Water Impact of Symmetric Wedges with a Multi-Material Eulerian Formulation,

International Journal of Maritime Engineering, Volume 154, Part A4, pp 191-206, 2012b.
29. WANG, S., GUEDES SOARES, C. Slam induced loads on bow-flared sections with various roll angles, *Ocean Engineering*, 67:45-57, 2013.
30. WU, G.X. Hydrodynamic force on a rigid body during impact with liquid. *Journal of Fluids and Structures*, Volume 12, pp 549-559, 1998.
31. WU, G.X., SUN, H., HE, Y.S. Numerical simulation and experimental study of water entry of a wedge in free fall motion. *Journal of Fluids and Structures*, Volume 19, pp 277-289, 2004.
32. XU, L., TROESCH, A., VORUS, W.S. Asymmetric vessel impact and planning hydrodynamics. *Journal of Ship Research*, Volume 42, No. 3, pp 187-198, 1998.
33. XU, G.D., DUAN, W.Y.,WU, G.X. Numerical simulation of oblique water entry of an asymmetrical wedge. *Ocean Engineering*, Volume 35, pp 1597-1603, 2008.
34. YETTOU, E1-M., DESROCHERS A. and Y. CHAMPOUX. A new analytical model for pressure estimation of symmetrical water impact of a rigid wedge at variable velocities. *Journal of Fluid and Structures*. Volume 23, pp. 501-522, 2007.
35. ZHAO, R., FALTINSEN, O.M. Water Entry of Two-Dimensional Bodies. *Journal of Fluid Mechanics,* Volume 246, pp 593-612, 1993.
36. ZHAO, R., FALTINSEN, O.M., AARSNES, J.V. Water entry of arbitrary two-dimensional sections with and without flow separation. *Proc. 21st Symposium on Naval Hydrodynamics*, pp 408-423, 1996.
37. ZHU, X.Y., FALTINSEN O.M., HU C.H. Water entry loads on heeled ship sections. *Proceedings of the 16th international conference on hydrodynamics in ship design*, Gdansk. pp. 407-416, 2005.

